NBSIR 74-512 (R)

The Proof Testing of Porcelain Insulators and the Application of Acoustic Emission

A. G. Evans, S. M. Wiederhorn, M. Linzer and E. R. Fuller, Jr.

Inorganic Materials Division
Institute for Materials Research
National Bureau of Standards
Washington, D. C. 20234

June 1974

Final Report

Evans, A. G., Wiederhorn, S. M., Linzer, M.,
Fuller, E. R., Jr., Proof testing of
porcelain insulators and application
of acoustic emission, Am. Ceram. Soc. Bull.
54, No. 6, 576-581 (June 1975).

313 NBSIR 74-512(R)

NBSIR 74-512

THE PROOF TESTING OF PORCELAIN INSULATORS AND THE APPLICATION OF ACOUSTIC EMISSION

A. G. Evans, S. M. Wiederhorn, M. Linzer and E. R. Fuller, Jr.

Inorganic Materials Division
Institute for Materials Research
National Bureau of Standards
Washington, D. C. 20234

June 1974

Final Report

ABSTRACT

An investigation of proof testing has been conducted on large
cone and post porcelain insulators. The cone configuration was found
to be unsuitable for overload proof testing to the loads needed for
effective lifetime predictions. The only merit of subjecting this
configuration to a proof test is the assurance of no immediate
macrocracking during installation. This is achieved by testing to
a load marginally larger than the service load. Conversely, the
post configuration was found to exhibit the basic prerequisites for
effective proof testing; but detailed stress analysis of this system is
needed before specific proof testing procedures can be recommended.
Finally, acoustic emission measurements were found to be a major
asset for monitoring both macrocracking events and stress development
during the proof tests.

1. INTRODUCTION

Macrocrack formation has been observed by the Navy in a number of the porcelain base insulators used to support large radio communications towers. These cracks do not, per se, impose a severe structural limitation because the primary stresses in the insulator are compressive. But, in the presence of the high voltage R.F. fields, the heat generated around the cracks may lead to structural degradation. Hence, towers containing cracked insulators are shut down. The prevention of macrocrack formation in porcelain base insulators is thus a primary requirement, if continuous operation (of the radio towers) is to be achieved.

One approach that can be used to prevent in-service macrocrack formation in ceramic components is overload proof testing. This is an evaluation procedure which subjects the insulator to a load greater than the service load. Then, if the insulator survives the proof test, it should satisfy engineering requirements of service load and lifetime. [1] The proof test condition for components made of porcelain must take into account the subcritical crack growth that occurs in this material due to moisture in the environment. [2] Subcritical crack growth leads to a time dependence of the strength, and the time to failure is determined by the time necessary for a crack to grow from a subcritical to a critical size. [1] A mathematical framework for the proof testing of components made of materials that exhibit subcritical crack growth indicates that the important parameters in proof testing are: [1,3,4] the proof test load, the test environment and the loading cycle. In addition, for compressive proof testing, a failure criterion must be specified, because crack size criticality does not lead to complete fracture.

In this paper, the proof test approach is applied to two types of porcelain base insulators commonly used to support radio towers. The variables of the study are loading rate and proof test load. Particular emphasis is placed on the use of acoustic emission to detect crack growth and as an aid in the formulation of a failure criterion.

2

2. EXPERIMENTAL PROCEDURE

The two types of insulators studied are shown in Figures 1 and 2. the bell-shaped "cone" insulators (Figure 1) were approximately one meter in height and one meter in diameter at the base. They were hollow, with a wall thichness at the base of approximately 0.08 m. The ends of the insulators were enclosed by steel end-caps, attached by Portland cement. The bottom bearing surface and the side surfaces of the porcelain were glazed, but the top bearing surface was not. The insulator was designed for a maximum compressive force of 13.5 MN.[*]

The "post" insulators (Fig. 2) were solid and cylindrical in shape, with circumferential skirts for improved electrical insulation. They too had steel caps at the top and bottom, attached by Portland cement. These insulators were designed for a maximum compressive force of 4.5 MN.

Tests were conducted using the 50 MN NBS test facility. A universal joint was placed at the top of each insulator to reduce loading eccentricities, and strain gauges were placed around the circumference to check on the uniformity. Loading and unloading times were varied from several seconds to approximately 1 hour. Tests were conducted in air (approximately 50 percent relative humidity). A total of four insulators were tested, two of each configuration.

The proof test load was established from a design diagram, developed earlier from subcritical crack growth studies on porcelain specimens cut from a similar cone insulator. [2] The design diagram (Fig. 3) gives a logarithmic plot of the minimum expected time to failure, t_{min}, versus the service stress, σ_a. Each straight line on this figure relates σ_a to t_{min} for a predetermined value of the proof ratio, i.e. the ratio of the proof stress (σ_p) to the service stress. Once a tentative determination is made of both the service stress and the minimum acceptable time to failure, the proof ratio can be determined form Fig. 3. For the cone insulators the maximum tensile stress at the service load (4.5 MN), as determined by finite element stress analysis, [5] is ~ 30 MN m^{-2}.

---

[*] 1 MN = 2.4×10^5 lbf.

3

Therefore, for a minimum service lifetime of 40 years, the requisite proof ratio obtained from Fig. 3 is 2.5, giving a proof load of 11.3 MN.

As noted in the preceding section, insulator "failure" has essentially occurred when macrocracks develop that are large enough to result in excessive heat generation, at the crack, during service. Since these cracks are mechanically stable and often do not appear at the external surface, a nondestructive means of detecting their presence was required. The two detection methods used in this study were ultrasonic pulse echo and acoustic emission. Each of the insulators was inspected ultrasonically* before and after each load cycle to detect the presence of macrocracks. Acoustic emission transducers capable of detecting signals emitted in a frequency range close to 180 kHz were attached to the insulators and were monitored continuously during the test. Ultrasonic transducers were also attached to some of the insulators during the tests and were periodically excited in an attempt to detect cracking, and hence, to relate crack formation to the load level and the acoustic emission rate. After testing, the insulators were sectioned to confirm predictions made from acoustic emission observations and ultrasonic inspection, and to determine the source of fracture.

3. EXPERIMENTAL RESULTS

   3.1 Cone Insulator Tests

      a) First Insulator

The first of two cone insulators was tested to three different proof levels, 7, 11 and 16 MN, in order to assess the general features of the structural and acoustic emission response. The initial loading rate was rapid (∿0.45 MN/min) up to approximately 60 percent of the proof load, and then reduced to ∿0.14 MN/min for the final load increment. The insulator was unloaded at ∿0.9 MN/min. Strain gauges located at

---

*
All ultrasonic testing reported in this paper was performed by Naval Research Laboratory personnel under the direction of S. Hart.

intervals of 120 degrees around the circumference at the mid-height
indicated that the strains were within 3 percent of the average strain.[*]

In all three cycles the acoustic emission rate increased during
loading, decayed during holding periods, but increased again as the
load was reduced. The increase on unloading was minimal for the 7 MN
test cycle, but rather substantial for the other two cycles, as depicted
in Fig. 4 for the 11 MN cycle. For this latter cycle (Fig. 4), the
acoustic emission rate increased slowly between 11 MN and 1 MN (from
10^3 to 3×10^3 counts/s); but below 1 MN, the rate increased rapidly,
and reached a maximum of 3×10^4 counts/s at zero load. This order
of magnitude increase in the acoustic emission rate probably corresponded
to the growth of a large internal crack, which was identified after
the proof test by ultrasonic inspection, and later by sectioning.
Visual inspection after sectioning showed that the crack initiated
at the bearing surface between the porcelain and the metal end cap, and
propagated approximately 0.15 m below the lip of the end cap and approxi-
mately one-third of the way around the circumference.

Crack formation and acoustic emission were even more apparent during
the proof test cycle to 16 MN (which was 2.5 MN above the compressive
strength reported by the manufacturer). As the load was increased above
13 MN peaks of continuous acoustic emission were obtained (i.e., an
acoustic emission rate $>10^5$ counts/s); similar, but more extensive,
peaks were noted when the insulator was unloaded. These emission peaks
probably corresponded to the growth of large cracks, which were identified
after the test by inspection. Visual inspection indicated that the
cracks initiated from the porcelain/cement bearing surfaces at the top
and bottom end caps. Cracks from the lower end cap frequently appeared
on the external surface.

5

The topology of the cracks was examined by ultrasonic and visual inspection after testing. Two principal types of crack were formed:[*] laminar cracks that grew from the top and bottom end caps roughly parallel to the exterior surface, and orthogonal cracks that grew through the insulator wall perpendicular to the exterior surface. An example of a laminar crack that emerged at the exterior surface is shown in Fig. 5. By sectioning the insulator we were able to show that this type of crack grew from the sloped bearing surfaces at the base and top of the insulator (Fig. 6). The rough surfaces of the laminar cracks served as nucleating sites for the longitudinal through cracks, shown in Fig. 7.

b) Second Insulator

The proof test of the second cone insulator was designed in an attempt to establish a specific proof test procedure that would provide an effective lifetime assurance. Two load cycles were used, differing only in the rate of load application; the maximum load in both cases being 7 MN. In the first cycle, the loading and unloading rates were 0.14 MN/min. In the second cycle, the loading rate was 0.9 MN/min and the average unloading rate was approximately 7 MN/min. Ultrasonic transducers were attached to the external surface of the insulator to detect the growth of cracks during the test. Strain gauges located 120 degrees apart around the circumference at the mid height were within 10 percent of the average strain.

---

[*] Other crack forms were observed in isolated cases; visual observation identified one circumferential crack orthogonal to the applied load, and ultrasonic inspection indicated the presence of many small internal cracks after rapid unloading.

6

The acoustic emission rate slowly increased as the insulator was loaded and further increased as the insulator was unloaded (Fig. 8). A large acoustic emission peak was observed at 9 MN during unloading. This peak was shown to correspond to macrocrack formation by an ultrasonic inspection during the proof test, in which the back surface reflection under one of the transducers slowly disappeared and was replaced by a reflection approximately one-half the distance between the interior and exterior surfaces. Additional ultrasonic inspection after the proof test confirmed the existence of this crack, which extended one-third of the way around the circumference and approximately 0.15 m below the upper end cap. The second proof test cycle resulted in saturation level acoustic emission rates ($>10^5$ counts/s) when the specimen was unloaded. Ultrasonic inspection of the cone insulator after testing detected no additional large cracks, but many small reflections were detected suggesting the nucleation and growth of many small cracks throughout the body of the insulator.

3.2 Post Insulator Tests

a) First Insulator

The first of the two post insulators was tested to several loads, 3, 4.5, 5.4, 6.3 and 8 MN in order to assess the basic structural and acoustic emission response of the configuration. Axial strains measured by four strain gauges placed 90 degrees apart around the circumference at the mid height of the insulator were within 7 percent of the average load at 3 MN. In the first cycle, the insulator was loaded to 3 MN at a rate of 0.14 MN/min and unloaded at a rate of 0.16 MN/min. A gradual increase in the acoustic emission rate accompanied the load increase (Fig. 9) and a decrease was observed when held at the proof load. But, the acoustic emission rate decreased during unloading (Fig. 9), a behavior which differs from that observed on the cone insulators. Ultrasonic examination after the proof test gave no indication of macro-crack formation.

The acoustic emission behavior at proof test loads of 4.5 and
5.4 MN was in general* similar to that observed for the test at
3 MN. The acoustic emission level increased as the load increased, but
decreased both during the holding and unloading periods. During the proof
test to 6.3 MN, acoustic emission peaks were observed during loading and
unloading, and subsequent visual inspection showed that some spalling
occurred at the lower insulator skirts. Finally, when the insulator
was loaded to 8 MN extensive acoustic emission was observed. But, gross
fracture did not occur until it was unloaded; then, at a load of 7 MN, the
skirts completely spalled off and longitudinal cracks running the length
of the insulator were formed, as shown in Fig. 10 (resulting in an
abrupt load decrease from 7 MN to 6 MN). The formation of these massive
cracks was preceded by a rapid increase in acoustic emission, for a
period of about 5 seconds before the observable event.

    b)   Second Insulator

        The second post insulator was subjected to a single load cycle,
up to 3 MN, in an attempt to establish an effective proof test. The
axial strains from the four strain gauges were within 13 percent of
the average strain at 3 MN. This insulator was loaded at a rate of
0.18 MN/min to 3 MN; the initial unloading (to 2 MN) was conducted
rapidly, at an average rate of 3 MN/min, and then continued at a
substantially reduced rate (0.18 MN/min) to zero load.

        The acoustic emission from the second post insulator is also
shown in Fig. 10. Again the acoustic emission rate increased as the load
increased, and decreased during unloading; but the decrease was marginal
in the rapid unloading regime (from 3 to 2 MN), which contrasts with the
continuous decrease observed during slow unloading in the first post
insulator. An untrasonic inspection of the post insulator after testing
gave no indication of macrocrack formation.

---

* An acoustic emission peak was noted at 4 MN. However, this cracking
did not represent the general behavior of this insulator configuration
because visual inspection showed that the cracking initiated from a
portion of one of the skirts that had been damaged before testing.

4. DISCUSSION OF RESULTS

The proof tests described in the preceding section have generated
important information about two aspects of the insulator proof test
procedure; (a) the use of acoustic emission to monitor crack
propagation, and (b) the lifetime assurances that can be provided by
proof testing. These features of the proof test are discussed for both
insulator configurations.

4.1 Acoustic Emission

Acoustic emission during proof testing can result from:
(a) plastic deformation in the steel end caps, (b) frictional effects
between the porcelain and cement, or (c) microcrack formation and
macrocrack growth in the porcelain (or cement). It is clearly very
important that an appreciation of the emission expected from each of
these sources be developed before attempting to analyze the acoustic
emission data.

4.1.1 Plastic Deformation

Plastic deformation results in intense acoustic emission
if the dislocations move in discrete glide "packets". [6] This occurs
only during the initial loading period when new dislocation sources are
being generated, and the acoustic emission due to a deforming part will
typically exhibit the features shown in Fig. 11. Deformation of the
steel end caps might, therefore, contribute to the emission during
initial loading, but is unlikely to be a significant contribution
during the constant load and unloading portions of a proof test cycle.

4.1.2 Frictional Effects

During proof testing slippage may occur at the porcelain/
metal/cement interfaces. Slippage will be particularly severe for
cone insulators because the bearing surfaces are not orthogonal to
the applied load. Similar slippage behavior might be expected during
loading and unloading, although the amplitude will be somewhat reduced
during unloading if the slippage is partially irreversible. Thus,
some of the acoustic emission observed in proof tests of cone insulators
can almost certainly be attributed to frictional effects during slippage.
By contrast, we shall see later (Section 4.1.4) that frictional effects
are unlikely to be the major source of acoustic emission in tests conducted
on the post insulators

9

4.1.3 Macrocrack Growth

Acoustic emission during macrocrack growth in porcelain has been investigated by Evans and Linzer. [2] They showed that the acoustic emission rate is approximately proportional to the crack velocity, (Fig. 12). A direct comparison between their acoustic emission data and the data in this paper is not possible, due to differences in specimen shape and size, the transducer location etc.; but their data illustrate the important trends needed for the qualitative analysis of macrocrack growth. A quantitative treatment can be performed and some objective conclusion reached with a modest amount of additional information (see Appendix).

Cracks that initiate in the tensile zones[*] of the cone insulator (type A zones) arrest in the structure, because they invariably propagate into adjacent compressive[*] zones (type B zones). The tensile stresses that aid crack growth are greatest at the top and bottom bearing inter-faces, decrease with distance from the interface, and finally become compressive approximately 0.15 m away. The crack growth rate is thus expected to exhibit an initial increase in zone A, reach a maximum value (see Appendix), and then decrease in zone B essentially to zero.

As the crack velocity increases from zero to a maximum, the acoustic emission rate must also go through a maximum. Hence, a peak in the acoustic emission rate is expected when macrocrack growth occurs.

Peaks of this sort were observed in the cone insulators (Figs. 4 and 8) and correlated with macrocrack formation. No significant peaks were observed during the simulation proof test in the post insulators.

---

[*] The terms tensile zone and compressive zone are used here to describe the regions in the insulator prior to macrocrack development in which the largest normal stresses orthogonal to the observed crack propagation planes are, respectively, tensile and compressive; hereafter, these regions are referred to as zones A and B, respectively.

An estimate of the proportionality constant relating the acoustic emission rate and crack velocity can be determined for the cone insulators from the maximum acoustic emission rate and the time taken for macrocrack growth. The maximum acoustic emission rate during the peaks was approximately 10^5 counts/s; the duration of the peaks was approximately 50 s and the crack growth was approximately 0.2 m, giving an average crack velocity of 4×10^{-3} m/s. If we assume that the average velocity is not very different from the maximum velocity, the proportionality is 2×10^7 counts/m (see the Appendix for a more detailed illustrative analysis); whereas the data of Evans and Linzer obtained on small specimens gave 10^5 counts/m.

4.1.4 Microcrack Formation

It has been shown [2] that microfracture of quartz particles in porcelain is a profuse source of acoustic emission; and that the rate of acoustic emission depends on the rate at which the quartz particles break. The dependence of acoustic emission rate on stress and time has been quantified for several loading conditions. [2] These results are expanded in a companion paper [7] to give the acoustic emission rate, dN/dt, for a constant stress rate, $\dot{\sigma}_L$, constant stress, σ_p, and constant unloading rate, $\dot{\sigma}_u$. For a constant stress rate, $\dot{\sigma}_L$, the acoustic emission rate (dN/dt) due to particle fracture for a homogeneous stress σ, except for stresses close to zero, is: [7]

$$\log (dN/dt) = \{[m(n+1)/(n-2]-1\}\log \sigma + \{1-[m/(n-2)]\} \log \dot{\sigma}_L + \phi \quad (1)$$

where m is the shape parameter for the quartz particle fracture stress distribution, ϕ is a constant, and n is the slow crack growth exponent (see Appendix). For a constant stress, σ_a, (following loading) the acoustic emission rate, except for very short times is: [7]

$$\log (dN/dt) = \{[m/(n-2)]-1\} \log t + \log (dN/dt)_L + \phi' \qquad (2)$$

where ϕ' is a constant and $(dN/dt)_L$ is the acoustic emission rate im-
mediately after loading is completed. For _unloading_, at a constant
rate, the acoustic emission rate except for stresses close to σ_a is: [7]

$$\log (dN/dt) = n \log (\sigma/\sigma_p)-[(n-m-2)/(n-2)] \log \{1+\phi''[1-(\sigma/\sigma_p)^{n+1}]\}$$
$$+ \log (dN/dt)_p \qquad (3)$$

where ϕ'' is a constant that depends on the loading, holding and unloading
times; and $(dN/dt)_p$ is the acoustic emission rate at the proof stress
immediately prior to unloading. These three relations can be used in
combination to predict the acoustic emission expected during a proof
test cycle, (Fig. 13), when the acoustic emission is due only
to microcrack formation. Alternatively, this source of acoustic emission
can be used as an approximate monitor of stress variations that may
occur in a component, due to unidentified or extraneous effects.

Some similarity between the predicted and observed emission rates
(Figs. 13 and 9) is apparent for the post insulators, suggesting that
acoustic emission in the post insulators is due mainly to microcrack
formation (occurring in the porcelain and/or the cement). A more
quantitative comparison can be made by using the acoustic emission test
data to calculate m and n of Eqs. (1) through (3). The slopes of
predicted curves in Fig. 13 are given by , $x = [m(n+1)/(n-2)]-1$, for the
constant loading rate portion of the curve and $y = [m/(n-2)]-1$ for the
constant stress portion. By substituting for x and y (the measured
values of these slopes), we find: $m \simeq 5$ and $n \simeq 10$. Similar values
were obtained in the laboratory on flexural specimens cut from an
equivalent insulator [2] (m = 3 to 4; n = 10 to 12), thus adding
additional credence to our suggestion that microcracking (occurring
mostly in the porcelain) is the primary source of acoustic emission
in these insulators.

The values of m and n can now be used to compute the acoustic
emission rate, due to microcracking, for a reversible, elastic system

during unloading. [7] The results for the post insulator, shown in Fig. 14, indicate an acoustic emission rate exceeding that expected for a reversible system. A similar calculation for the cone insulators would indicate a much larger discrepancy. This additional acoustic emission is almost certainly due to residual stress development (resulting from some irreversible slip at the porcelain/cement interface), which causes additional microcracking; and, for the cone insulators, leads to macrocrack formation. A mmeasure of the severity of the residual stress can be computed by substituting the observed acoustic emission rate on unloading into Eq. (3). [7] The result (Fig. 15) indicates a small, but significant, residual stress that persists to zero load.

4.2   Lifetime Assurance After Proof Testing

4.2.1 Cone Insulator

The observations of macrocracking and profuse acoustic emission during unloading of the cone insulators show that extensive irreverisble slippage occurs in this configuration at the porcelain/cement interfaces, which leads to substantial residual stress development during load release. The stresses that develop during unloading apparently exceed the stresses at the proof load. Hence, no realistic lifetime assurances after proof testing can be provided.

In systems that exhibit substantial irreversibility during proof testing the only merit of proof testing is the assurance that there will be no instantaneous failure during installation. This can be ensured by proof loading to a load just in excess of the service load (by say 5 percent). This load should then be maintained on the component until installation, using a clamping fixture, to avoid macrocracking in the period between proof testing and installation.

Finally, it is noted that although this proof test procedure gives no guarantee that all surviving insulators will resist in-service macrocracking, a proportion of the insulators will give a satisfactory in-service performance. The proportion that gives good performance

depends on the statistical nature of the flaw size distribution in the critical parts of the insulators, [1.4] i.e., near the top and bottom interfaces. The distribution function is difficult to obtain and is notoriously dependent on fabrication variables, [8] but approximate values could be obtained from a survey of the performance of insulators already in service.

4.2.2 Post Insulator

Residual stress development also occurs in the post insulators during unloading, but the stresses are comparatively modest, and not large enough to generate macrocracks. This configuration thus exhibits the basic features needed for effective lifetime assurances after proof testing.

Quantitative lifetime predictions after proof testing require values for the maximum stress during the proof test, σ_p, and the maximum stress during service, σ_a. [1] The ratio σ_p/σ_a then gives the minimum failure time from Fig. 3, if the stress distributions are comparable. [1,4] For a system that exhibits reversible behavior, this ratio is given directly by the ratio of the proof load to the service load. But, for a system that exhibits some irreversibility, this load ratio does not suffice. Instead, a detailed stress analysis (for the complete proof cycle and the service condition) is needed to obtain values for the maximum stress in the proof test, and its distribution, and the maximum in-service stress. This analysis has not been performed, and hence, we cannot yet determine whether an effective proof test procedure for this system is a practical feasibility. We suggest that urgent attention is devoted to this stress analysis (both analytically using stress calculations and empirically using acoustic emission) to enable this issue to be resolved.

5. CONCLUSIONS AND RECOMMENDATIONS

Proof test have been conducted on cone and post porcelain insulators. At the proof loads needed to guarantee approximately 40 hrs. lifetime

without macrocracking, extensive irreversible interface slippage occurs in the cone configuration, and this leads to macrocracking while unloading. This specific configuration is thus not capable of effective overload proof testing. It is recommended, therefore, that the insulators are only proof tested to a load just above the in-service load, if an assurance of no immediate "failures" during installation is required (and that nondestructive inspection is used to identify the proof test failures). No significant lifetime predictions can be provided for this insulator.

The post insulator can be subjected to the loads needed for effective overload proof testing without excessive slippage and without gross macrocracking. This configuration thus has the basic prerequisites for lifetime prediction after proof testing. However, the detailed prediction requires information about the stress distribution in these insulators, both during proof testing and in service. It is hoped that this information can be provided by stress analysis and acoustic emission measurements. Then it will be possible for proof test procedures to be developed.

Acoustic emission was monitored throughout the proof tests and was found to generate information about the two most crucial problems in insulator proof testing: internal stress development and macrocracking (the latter constituting a proof test failure in compression proof testing). Analyses have been presented which form the basis for the quantitative deter-mination of residual stress development and for the detection of macro-cracking events using acoustic emission. Acoustic emission measurements during proof testing thus permit a substantial extension of the proof testing technique to quantitative lifetime predictions, although more extensive calculations of acoustic emission rate are required to explore the full potential of the technique in this application. Finally, for future proof test studies, we recommend that a large acoustic emission system, employing several correlated transducers, is utilized. This would add an extra dimension to the study, by permitting spatial resolution of the acoustic emission sources.

15

APPENDIX

ACOUSTIC EMISSION DUE TO MACROCRACKING

Firstly, we need to obtain the relation between the stress intensity factor, K_I, and the crack length for the component. This is determined for a symmetrically loaded central through crack from the relation: [9]

$$K_I = 2 \left(\frac{a}{\pi} \right)^{1/2} \int_0^a \frac{\sigma_y}{(a^2 - x^2)^{1/2}} \, dx \qquad (A1)$$

where σ_y is the stress orthogonal to the crack plane and $2a$ is the crack length; this relation also applies, to a good approximation, for an edge crack of length a.

For illustration purposes we shall now consider an edge crack propagating in a linearly decreasing stress field (Fig1.16a):

$$\sigma_y = \sigma_t \left[1 - \frac{x}{a^*} \right] \qquad (A2)$$

where σ_t is the maximum tension in zone A and a^* is the size of zone A. Substituting σ_y in Eq. (A1) and integrating gives:

$$K_I = \sigma_t \sqrt{\pi a} \left[1 - \frac{2a}{\pi a^*} \right] \qquad (A3)$$

or, if we define K_o as the stress intensity factor for initial flaw propagation ($K_o = \sigma_t \sqrt{\pi a_o}$, where a_o is the initial flaw size) then:

$$K_I = K_o \sqrt{\frac{a}{a_o}} \left(1 - \frac{2a}{\pi a^*} \right) \qquad (A4)$$

Next, we shall differentiate to determine the maximum stress intensity factor, $(K_I)_{max}$; this gives

16

$$dK = \frac{K_o}{\sqrt{a_o}} \left[\frac{1}{2\sqrt{a}} - \frac{3\sqrt{a}}{\pi a^*} \right] = 0$$

so that $a = \pi a^*/6$ and:

$$(K_I)_{max} = \frac{2K_o}{3} \sqrt{\frac{\pi a^*}{6a_o}} \tag{A5}$$

Also, note that $K_I=0$, when $a=\pi a^*/2$. Hence, we can construct relatively simple (K_I, a) diagrams for this system, as depicted in Fig. 16b.

Now, the (K_I,a) relation can be combined with the (K_I,V) relation to obtain velocity, time diagrams, as follows;

Using, $V = AK_I^n$, for the slow crack growth relation [1] (where n and A are separate quantities for each region of crack growth), and combining with Eq. (A4) gives;

$$t = \frac{a_o^{n/2}}{AK_o^n} \int_{a_1}^{a_2} \frac{[1-2a/\pi a^*]^{-n}}{a^{n/2}} \, da \tag{A6}$$

where t is the crack propagation time. Expansion and integration then gives, for $a_2 >> a_1$;

$$t = \frac{2}{AK_o^n} \frac{a_o^{n/2}}{a_1^{n-2/2}} \left[\frac{1}{n-2} + \frac{n}{(n-4)} \left(\frac{2a_1}{\pi a^*}\right) + \frac{n(n+1)}{2(n-6)} \left(\frac{2a_1}{\pi a^*}\right)^2 + \ldots \right] \tag{A7}$$

For $2a_1/\pi a^* \stackrel{\sim}{<} n$, this becomes

$$t = \frac{2a_1}{AK_{Ii}^n(n-2)} \equiv \frac{2a_1}{V_1(n-2)} \approx \frac{2(K_{Ii})^2}{\pi \sigma_t^2 V_1(n-2)} \tag{A8}$$

where V_1 is the crack velocity when $a = a_1$. The total duration of the macrocracking event is obtained by putting $a_1 = a_o$ and $V_1 = V_o$. But, a more important quantity for the acoustic emission analysis is the duration which gives an acoustic emission rate in excess of the background. This is obtained by putting V_1 equal to the velocity, V', where the acoustic emission due to macrocracking exceeds the background emission; and a_1 becomes the corresponding crack length.

17

References

1. A. G. Evans and S. M. Wiedernorn, NBSIR 73-147 (March 1973), Intl. Jnl. Frac., in press.

2. A. G. Evans and M. Linzer, Jnl. Amer. Ceram. Soc. $\underline{56}$, 575 (1973).

3. A. G. Evans and E. R. Fuller, Mater. Sci. Eng., to be published.

4. S. M. Wiederhorn, Ceramics for High Performance Applications, in press.

5. A. H. Heuer, private communication.

6. A. S. Tetelman and A. G. Evans, Fracture Mechanics of Ceramics, $\underline{2}$, 895, (1974).

7. A. G. Evans, J. Am. Ceram. Soc., to be published.

8. A. G. Evans and T. G. Langdon, Progress in Materials Science, to be published.

9. S. Vaidyanathan and I. Finnie, Jnl. of Basic Engineering (ASME), June 1971, p. 242.
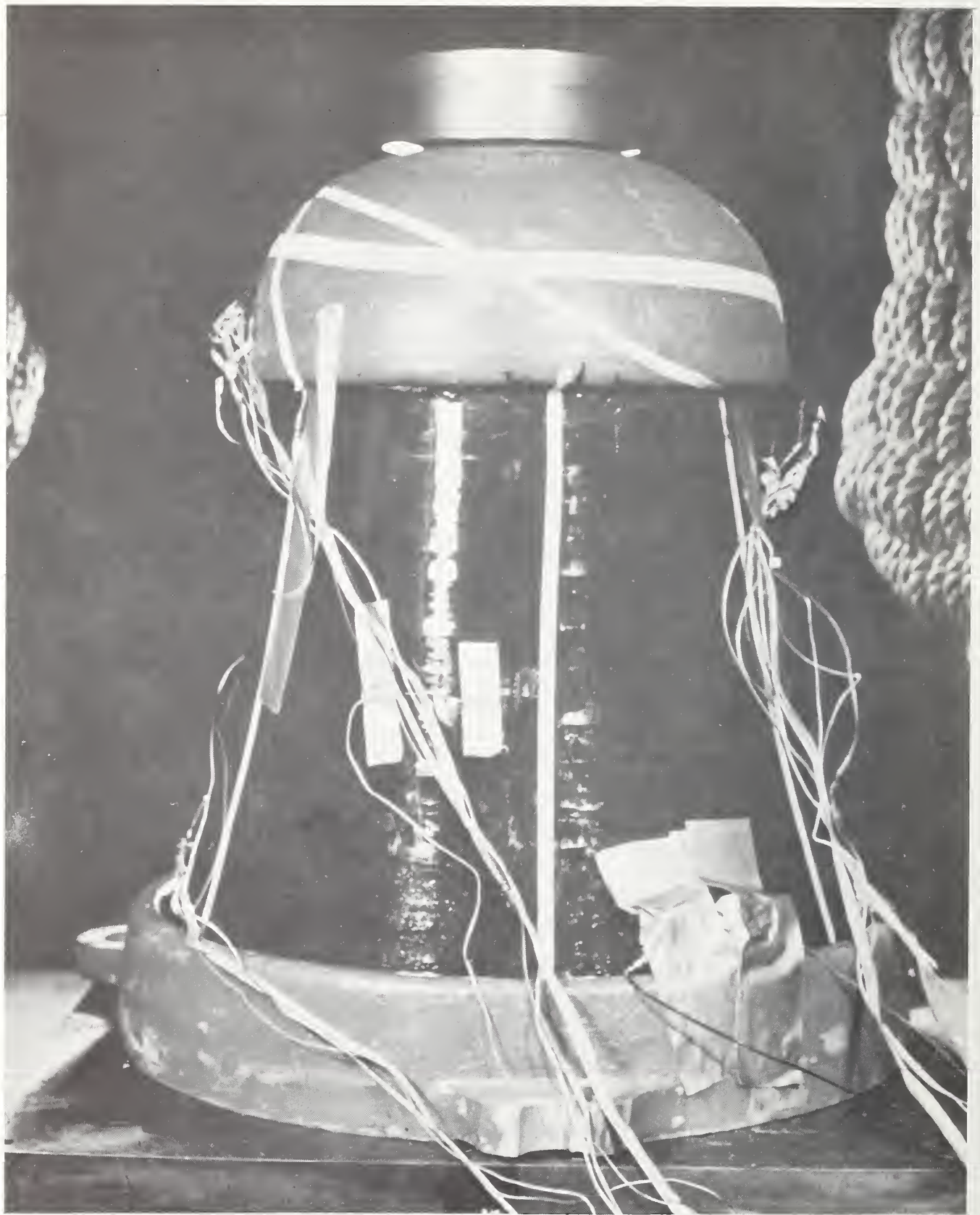
Fig. 1. A typical cone insulator used in this study.

Fig. 2. A typical post insulator used in this study.

Fig. 3. A proof test diagram for porcelain in humid environments[2], giving the minimum service life time as a function of the service stress, σ_a, at various proof stress levels, σ_p.

Fig. 4. The relation between acoustic emission rate and load obtained on a cone insulator loaded to 11 MN, and unloaded rapidly. The large rate increase during unloading (just prior to zero load) can be attributed to macrocrack formation.

Fig. 5. An example of a laminar crack formed in a cone insulator.
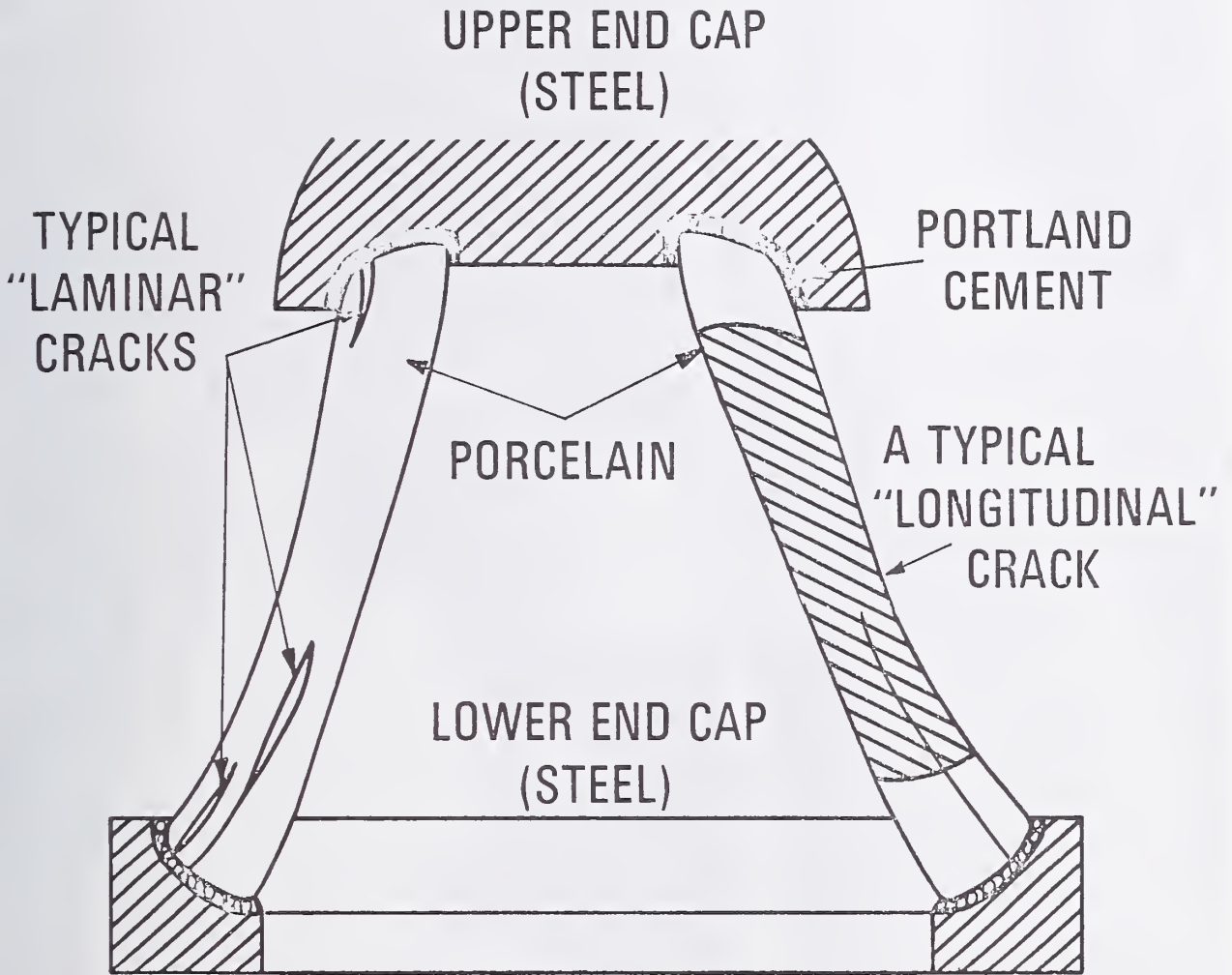
Fig. 6. A schematic of the laminar and orthogonal cracks that form in cone insulators.
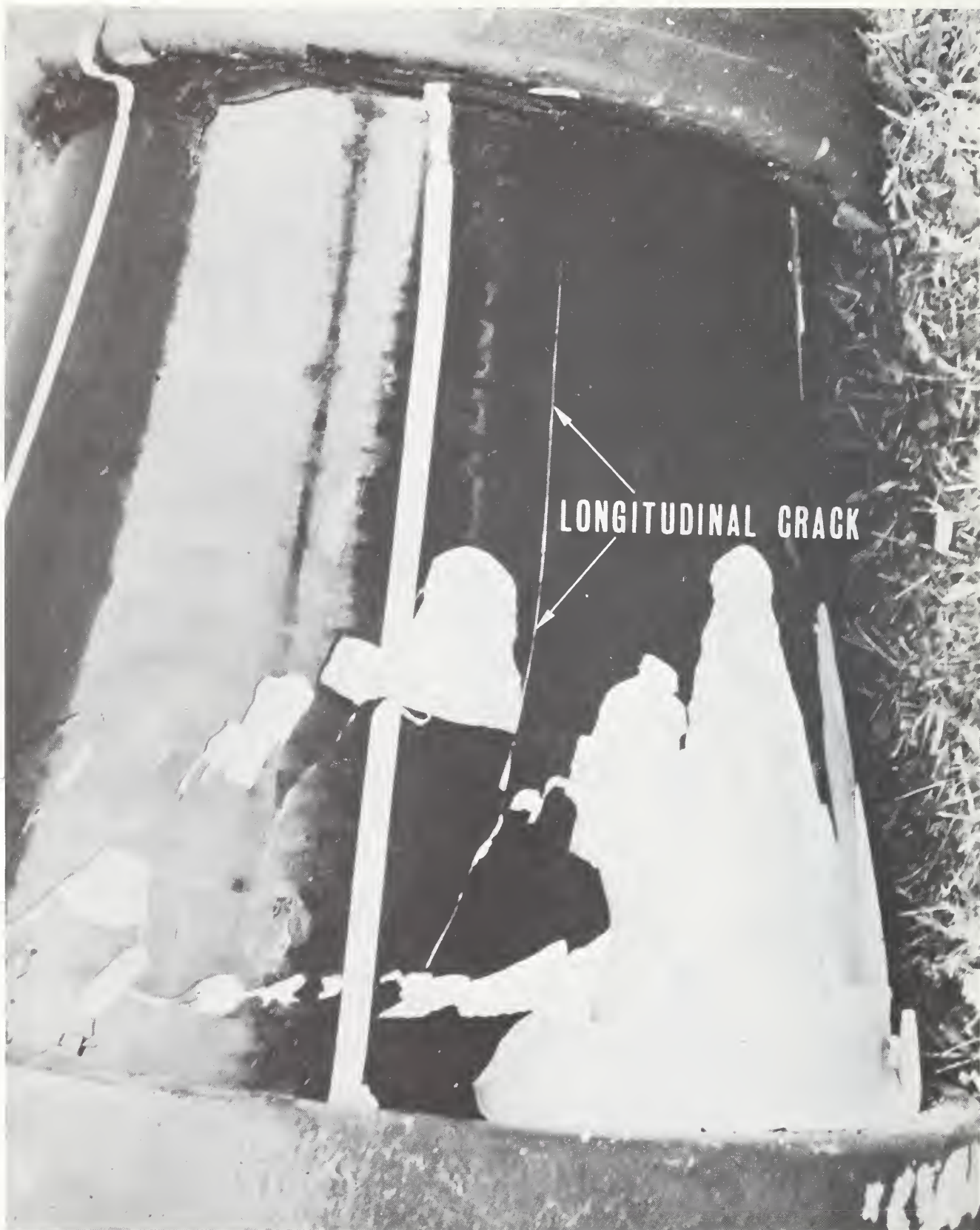
Fig. 7. An example of a longitudinal crack in a cone insulator.

Fig. 8. The acoustic emission rate obtained on a second cone insulator loaded to 11 MN and unloaded slowly. An acoustic emission peak appears during unloading at 9 MN, and has been attributed to macrocracking.

Fig. 9. The acoustic emission rates obtained on the post insulators during loading to 3 MN and unloading.

Fig. 10. A post insulator after testing to 7 MN and unloaded to 6 MN.

Fig. 11. The acoustic emission expected due to plastic deformation of the steel end caps.

Fig. 12. The relation between acoustic emission rate and crack growth rate during slow crack growth in porcelain.[2]

Fig. 13. The predicted acoustic emission rate from microcracking in an elastic, reversible system.

Fig. 14. A comparison of the acoustic emission rates measured during unloading with the rates predicted for a reversible, elastic system.

Fig. 15. The relative residual stress in the post insulators during unloading as predicted from the excess acoustic emission; σ_R is the residual stress and σ_p is the stress at the proof load.

Fig. 16. (a) A schematic of a linearly decreasing stress field defining the parameters used in the text.

(b) The relation between stress intensity factor, K_I, and crack length, a, for the stress field in Fig. 16 (a).

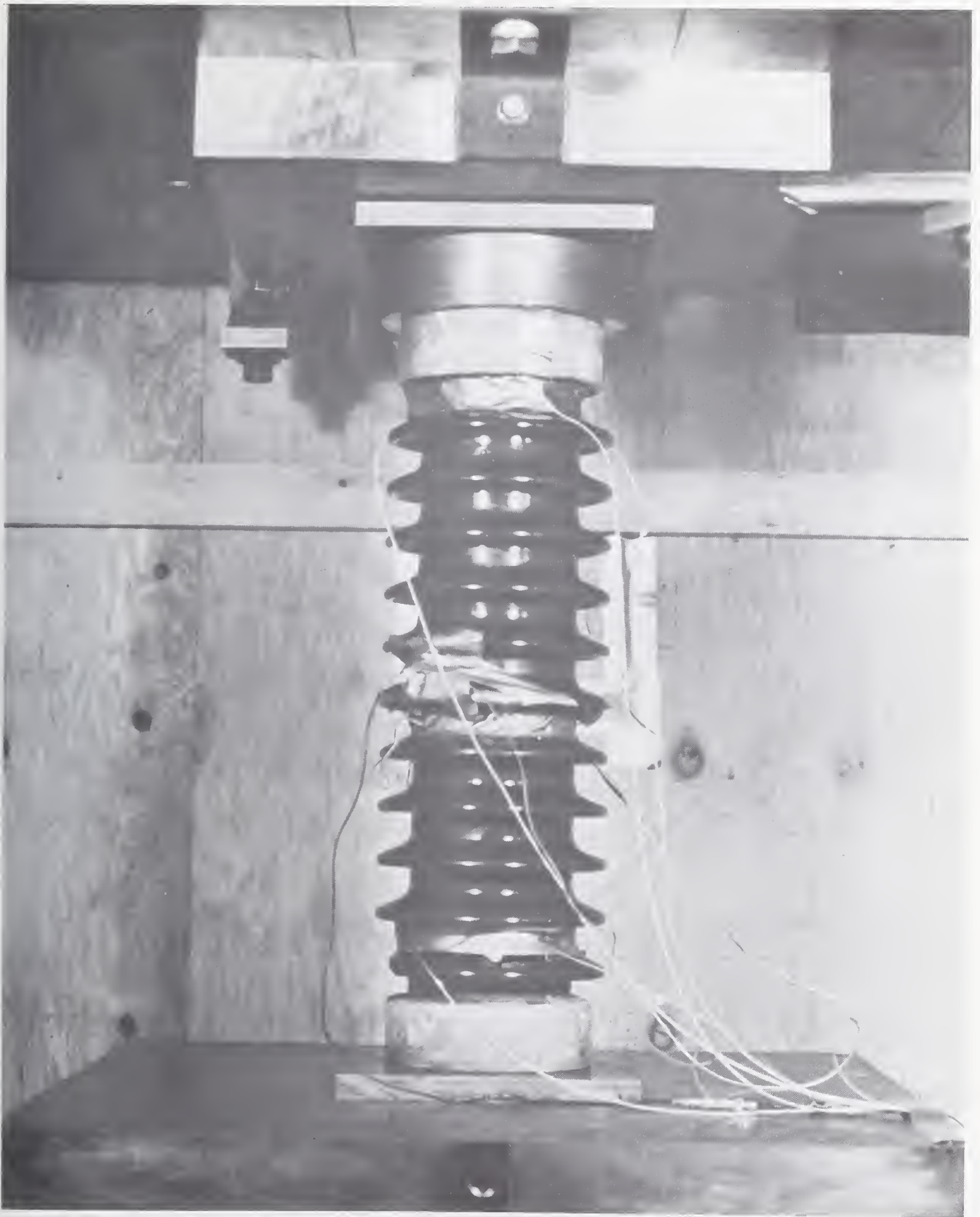Fig. 1.   A typical cone insulator used in this study.

Fig. 2.   A typical post insulator used in this study.
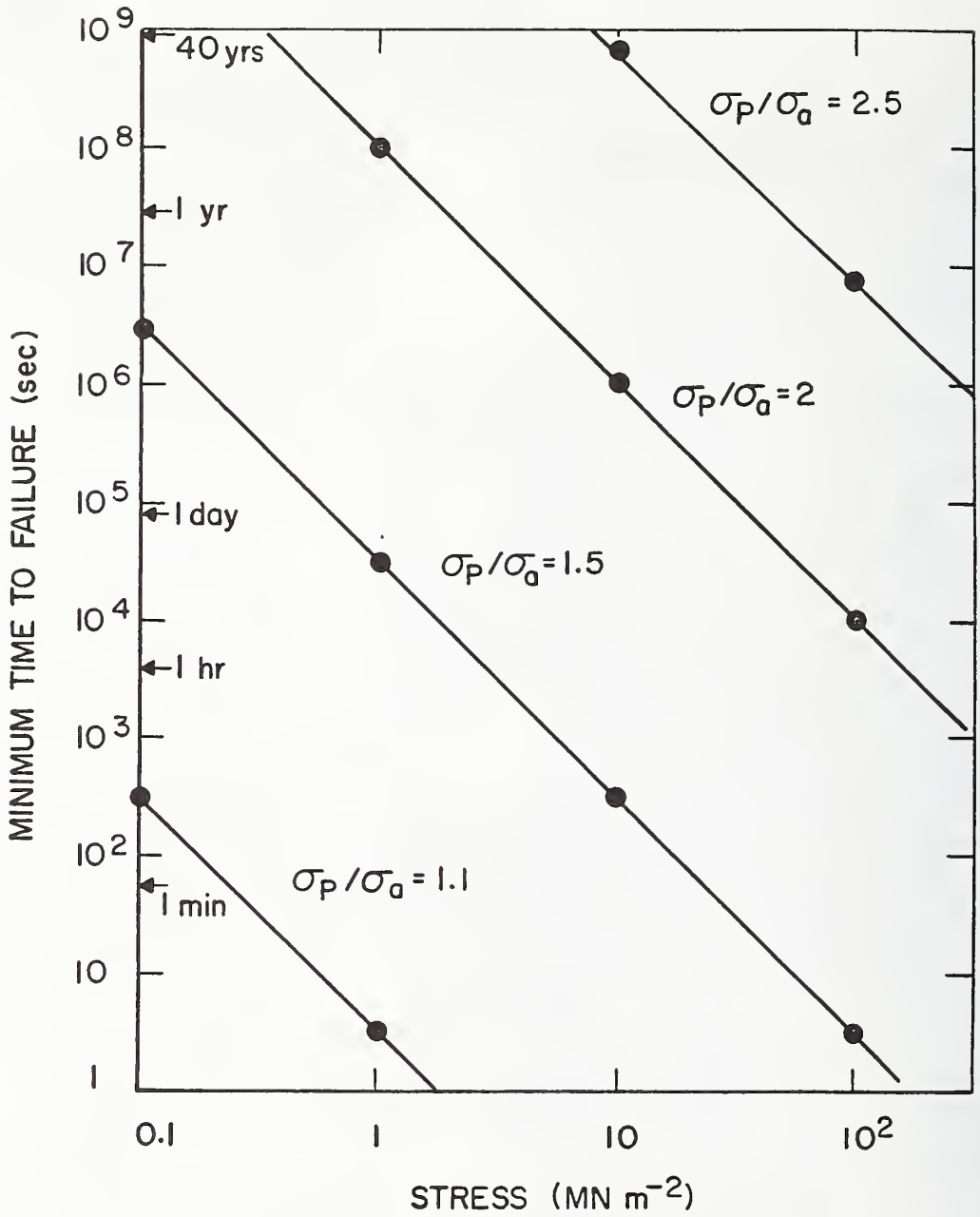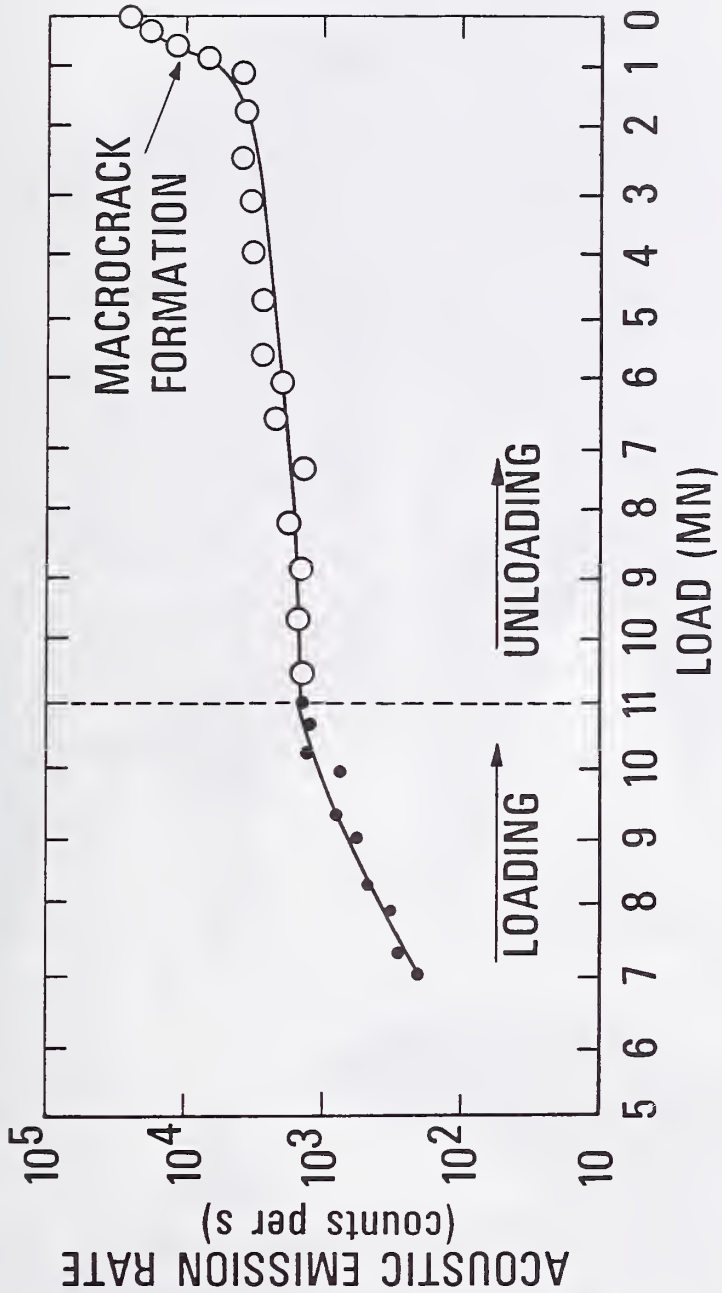
Fig. 3. A proof test diagram for porcelain in humid environments[2], giving the minimum service life time as a function of the service stress, σ_a, at various proof stress levels, σ_p.

22

Fig. 4. The relation between acoustic emission rate and load obtained on a cone insulator loaded to 11 MN, and unloaded rapidly. The large rate increase during unloading (just prior to zero load) can be attributed to macrocrack formation.

23

Fig. 5. An example of a laminar crack formed in a cone insulator.

UPPER END CAP
(STEEL)

TYPICAL
"LAMINAR"
CRACKS

PORTLAND
CEMENT

PORCELAIN

A TYPICAL
"LONGITUDINAL"
CRACK

LOWER END CAP
(STEEL)

Fig. 6.   A schematic of the laminar and orthogonal cracks that form
          in cone insulators.

25

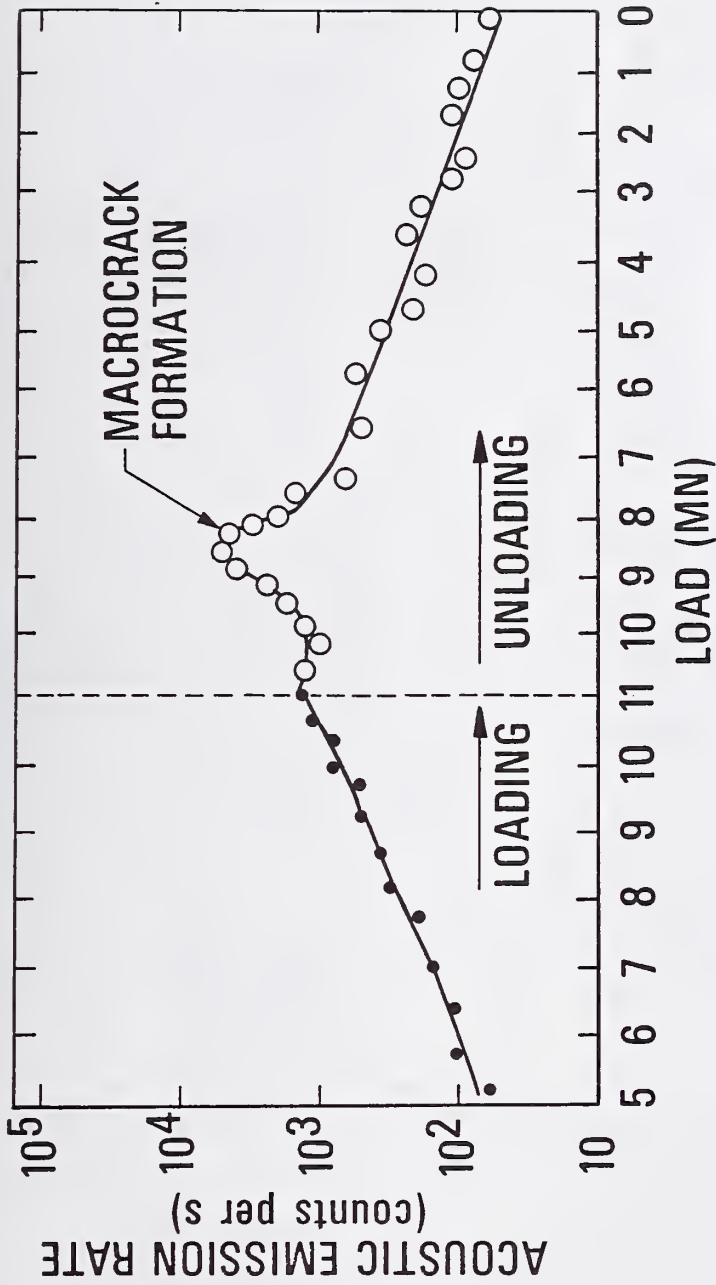Fig. 7. An example of a longitudinal crack in a cone insulator.

Fig. 8. The acoustic emission rate obtained on a second cone insulator loaded to 11 MN and unloaded slowly. An acoustic emission peak appears during unloading at 9 MN, and has been attributed to macrocracking.
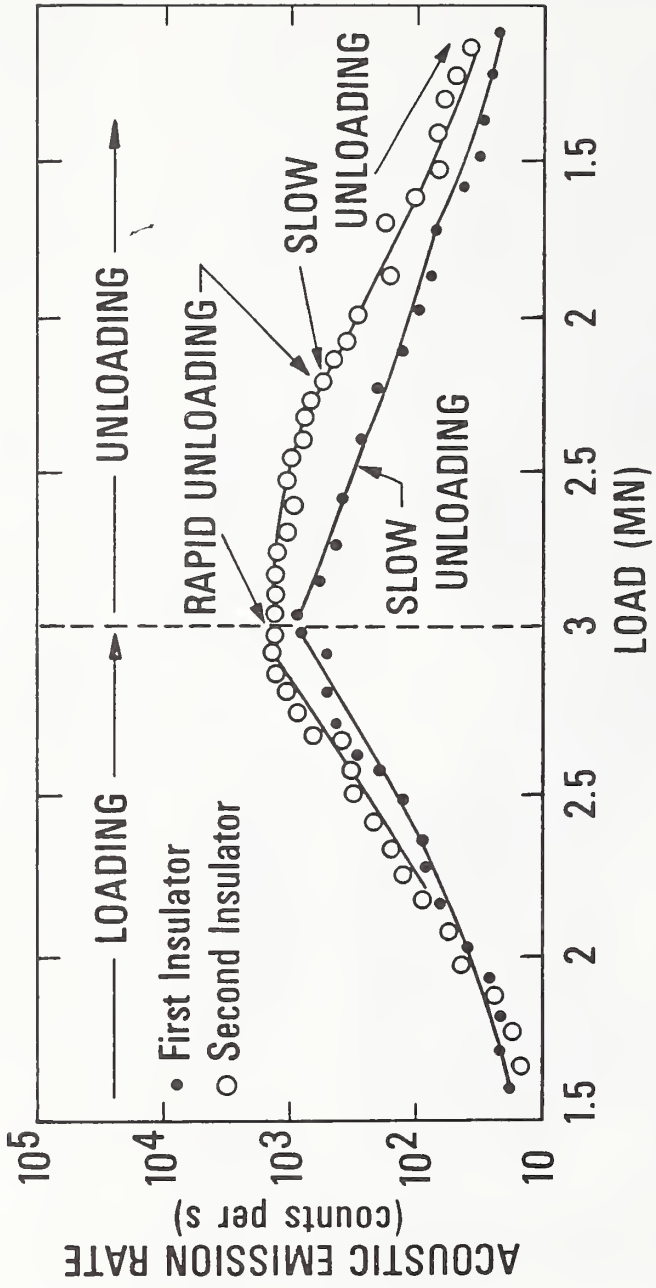
27

Fig. 9. The acoustic emission rates obtained on the post insulators during loading to 3 MN and unloading.

28

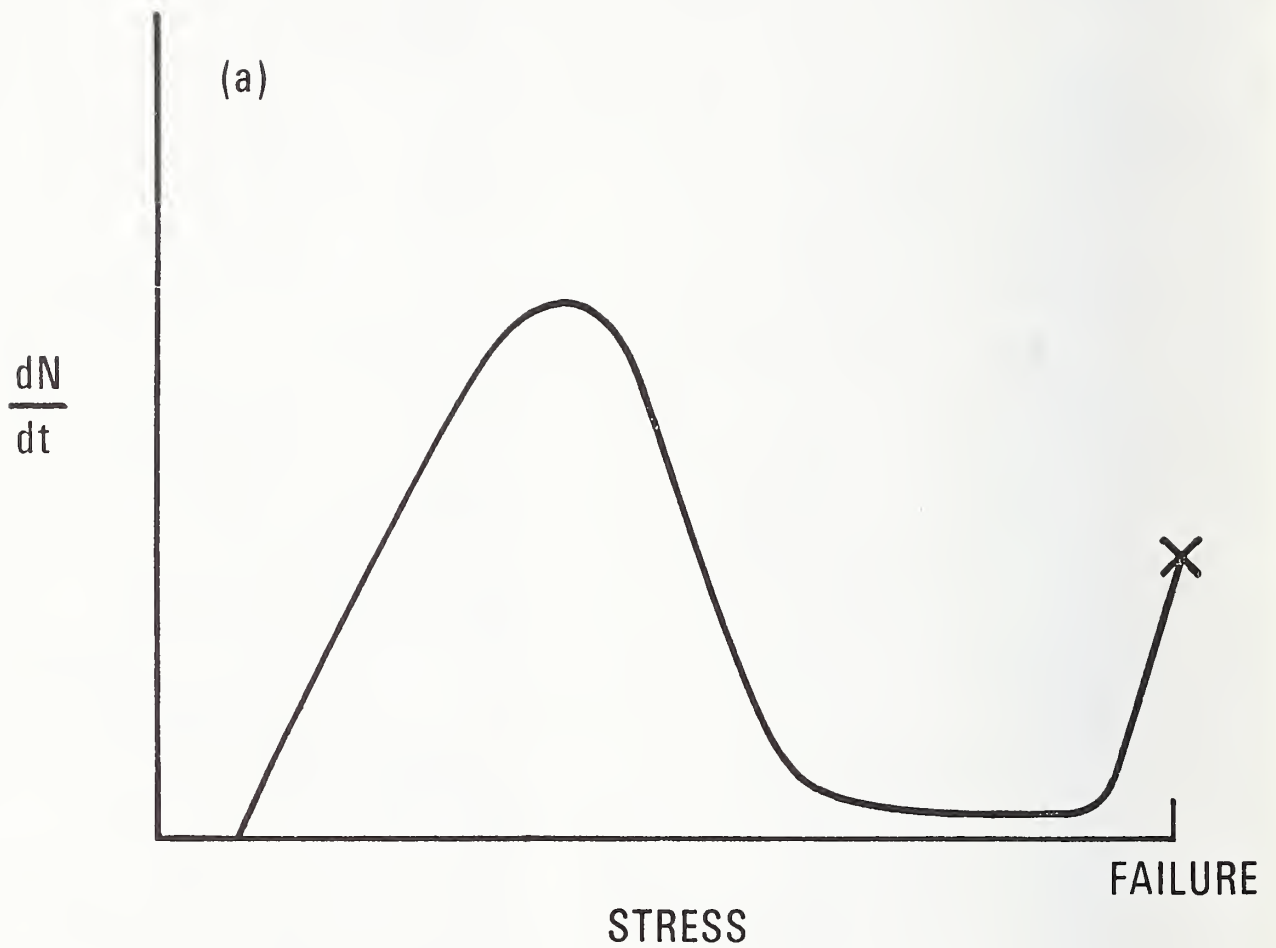Fig. 10. A post insulator after testing to 7 MN and unloaded to 6 MN.

Fig. 11.   The acoustic emission expected due to plastic deformation of the steel end caps.
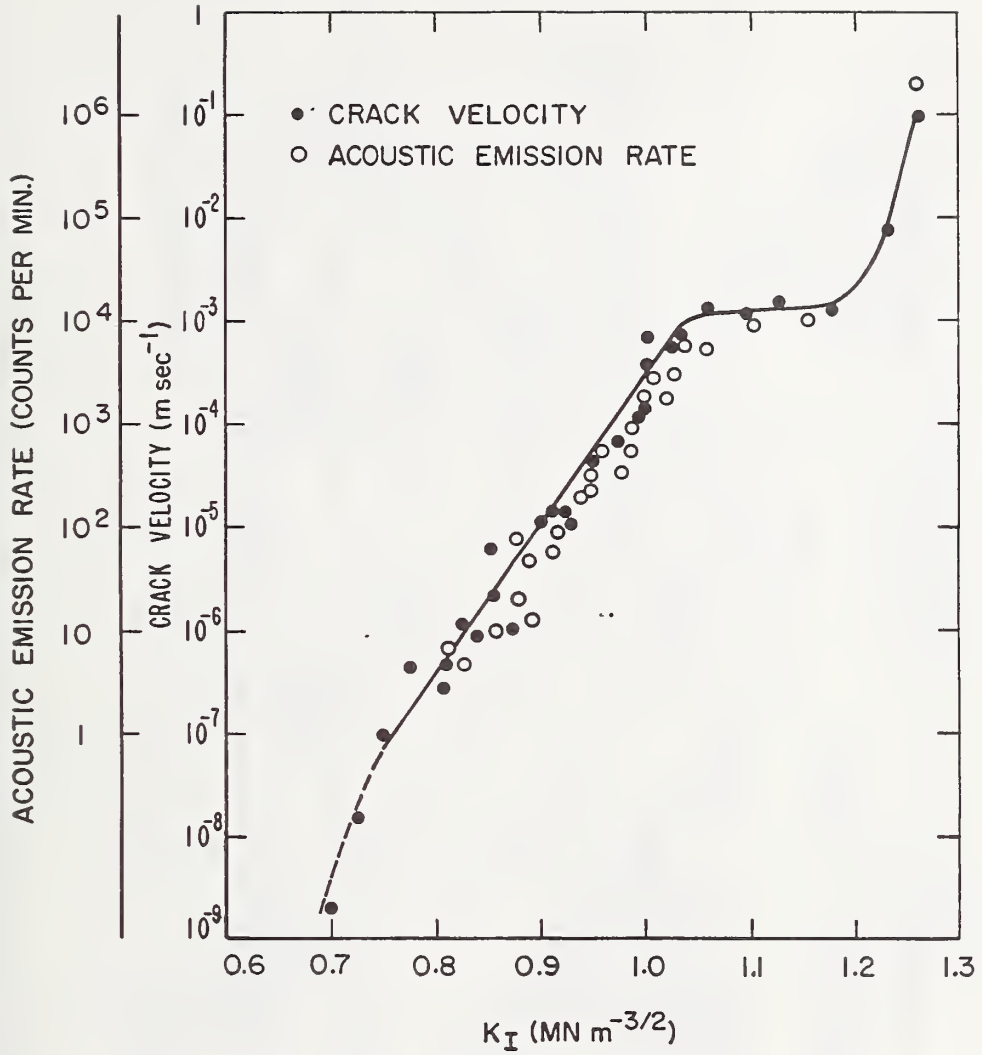
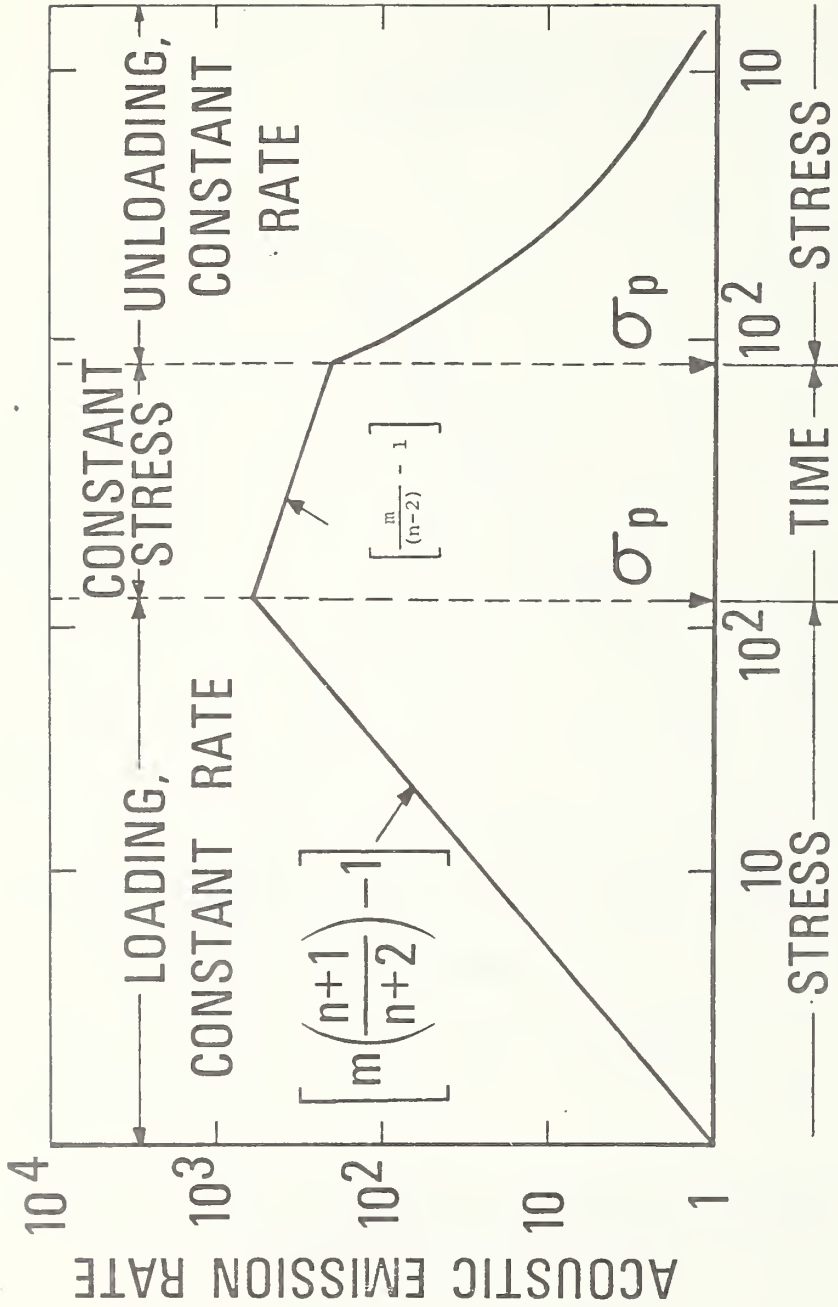Fig. 12. The relation between acoustic emission rate and crack growth rate during slow crack growth in porcelain.[2]

Fig. 13. The predicted acoustic emission rate from microcracking in an elastic, reversible system.
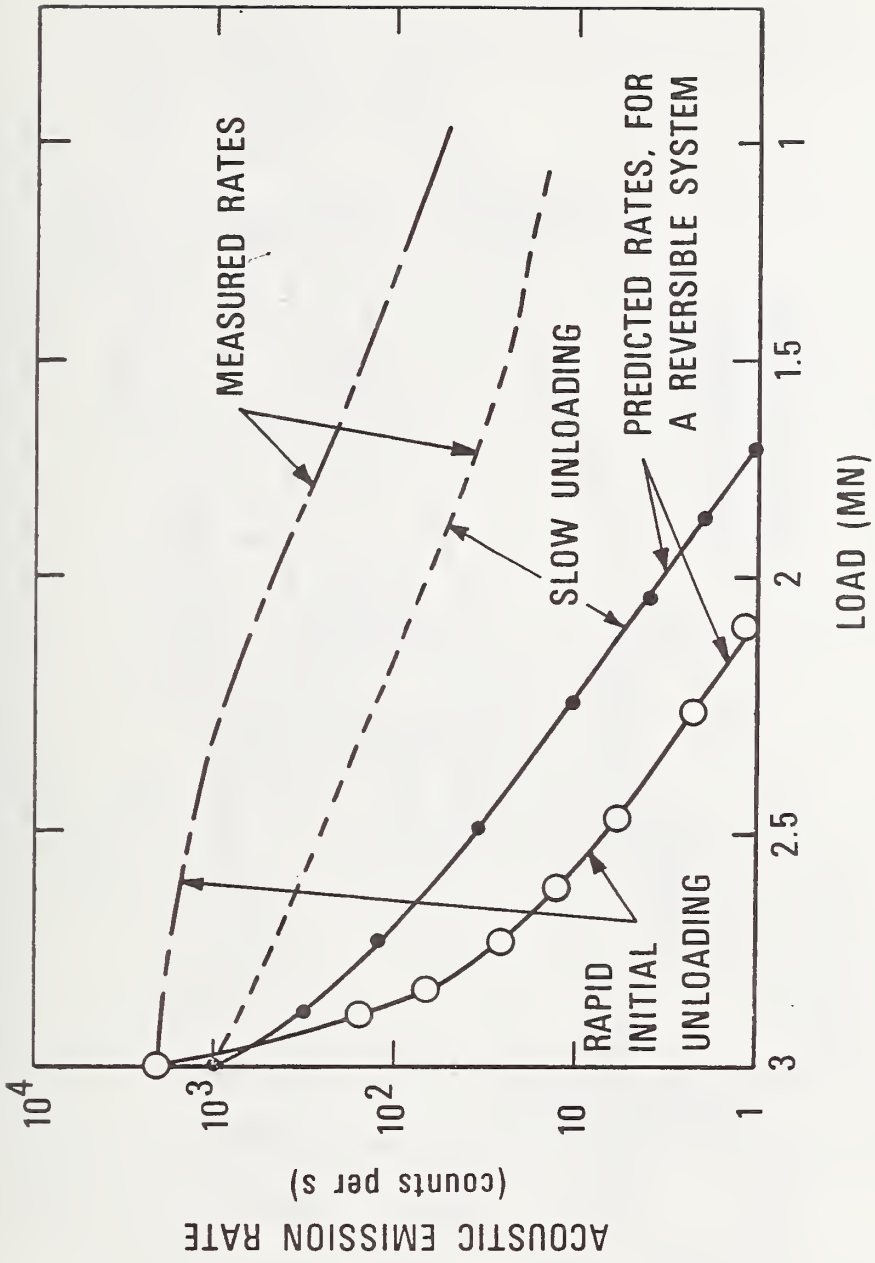
32

Fig. 14. A comparison of the acoustic emission rates measured during unloading with the rates predicted for a reversible, elastic system.
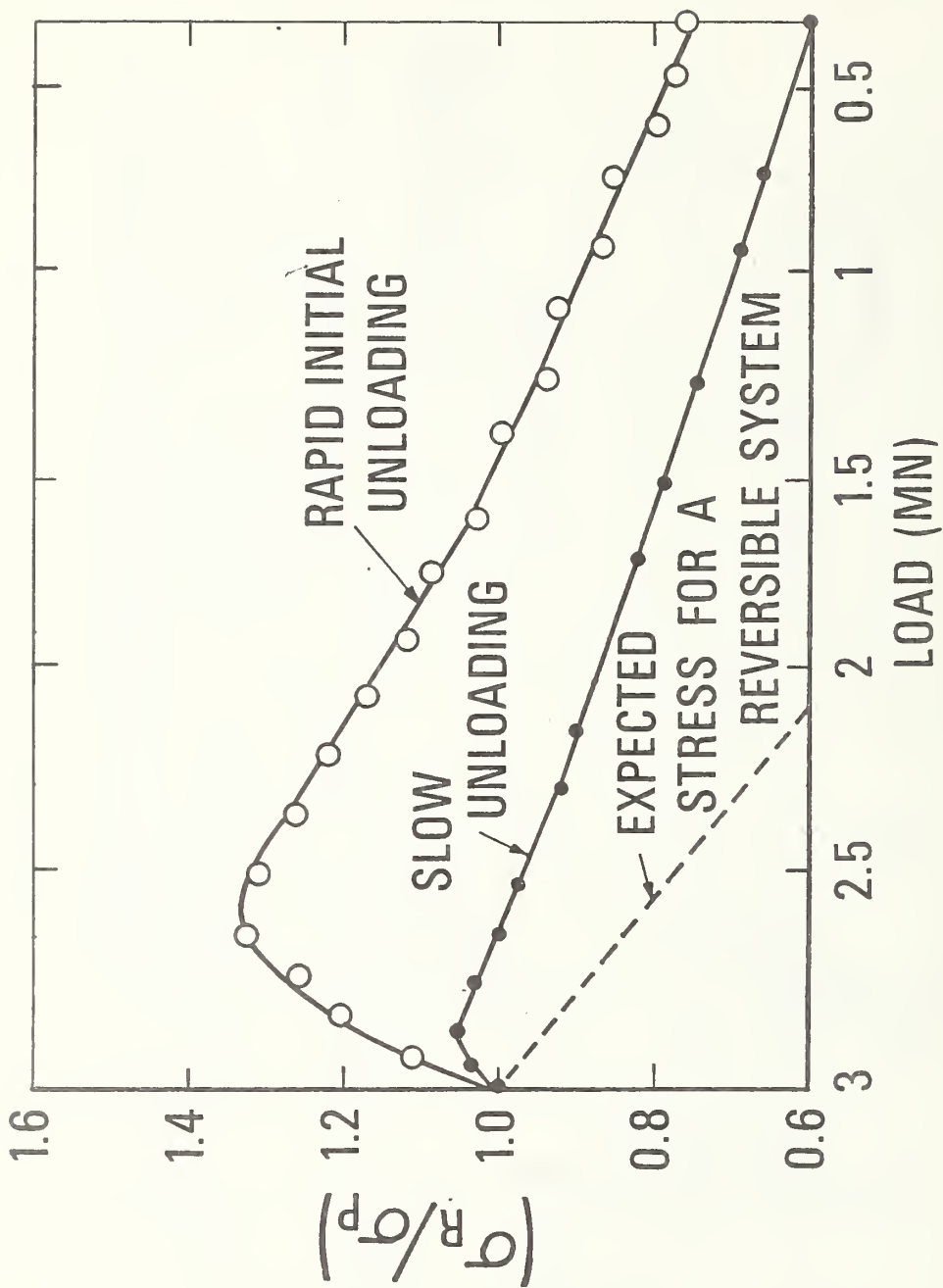
33

Fig. 15. The relative residual stress in the post insulators during unloading as predicted from the excess acoustic emission; σ_R is the residual stress and σ_P is the stress at the proof load.
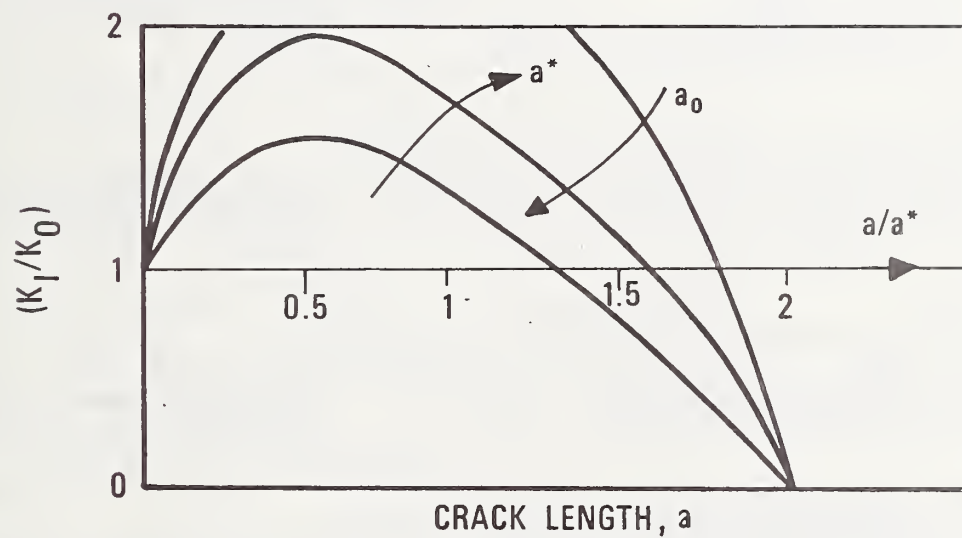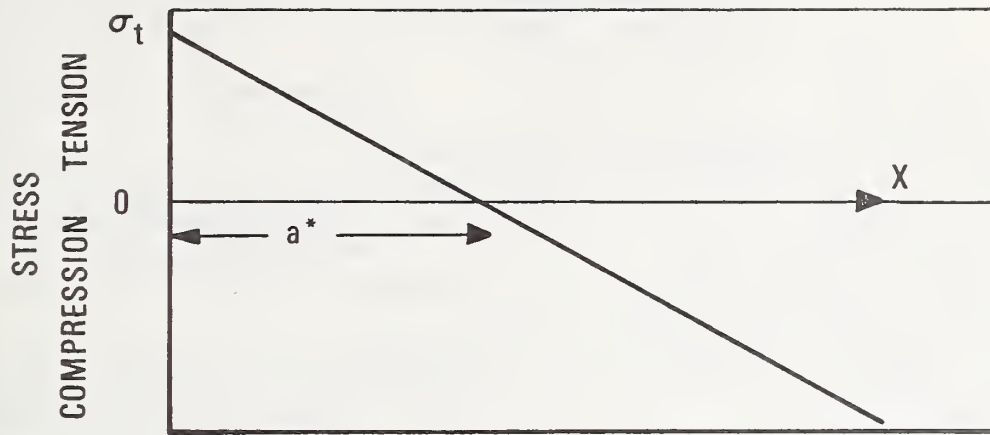
34

Fig. 16. (a) A schematic of a linearly decreasing stress field defining the parameters used in the text.

(b) The relation between stress intensity factor, K_I, and crack length, a, for the stress field in Fig. 16 (a).

DISTRIBUTION LIST

Organization

Office of Naval Research
Department of the Navy
Attn: Code 471
Arlington, Virginia 22217

Director
Office of Naval Research
Branch Office
495 Summer Street
Boston, Massachusetts 02210

Commanding Officer
Office of Naval Research
New York Area Office
207 West 24th Street
New York, New York 10011

Director
Office of Naval Research
Branch Office
219 South Dearborn Street
Chicago, Illinois 60604

Director
Office of Naval Research
Branch Office
1030 East Green Street
Pasadena, California 91101

Commanding Officer
Office of Naval Research
San Francisco Area Office
San Francisco, California 94102

Commanding Officer
Naval Weapons Laboratory
Attn: Research Division
Dahlgren, Virginia 22448

Organization

Director
Naval Research Laboratory
Attn: Technical Information Officer
        Code 2000
Washington, D. C. 20390

Director
Naval Research Laboratory
Attn: Technical Information Officer
        Code 2020
Washington, D. C. 20390

Director
Naval Research Laboratory
Attn: Technical Information Officer
        Code 6000
Washington, D. C. 20390

Director
Naval Research Laboratory
Attn: Technical Information Officer
        Code 6100
Washington, D. C. 20390

Director
Naval Research Laboratory
Attn: Technical Information Officer
        Code 6300
Washington, D. C. 20390

Director
Naval Research Laboratory
Attn: Technical Information Officer
        Code 6400
Washington, D. C. 20390

Director
Naval Research Laboratory
Attn: Library
        Code 2029 (ONRL)
Washington, D. C. 20390

Commander
Naval Air Systems Command
Department of the Navy
Attn: Code AIR 320A
Washington, D. C. 20360

Commander
Naval Air System Command
Department of the Navy
Attn: Code AIR 5203
Washington, D. C. 20360

Commander
Naval Ordnance Systems Command
Department of the Navy
Attn: Code ORD 033
Washington, D. C. 20360

Commanding Officer
Naval Air Development Center
Aeronautical Materials Div.
Johnsville
Attn: Code MAM
Warminster, Pa. 18974

Commanding Officer
Naval Ordnance Laboratory
Attn: Code 210
White Oak
Silver Spring, Maryland 20910

Commander
Naval Ship Systems Command
Department of the Navy
Attn: Code 0342
Washington, D. C. 20360

Commanding Officer
Naval Civil Engineering Laboratory
Attn: Code L70
Port Hueneme, California 93041

Commander
Naval Ship Engineering Center
Department of the Navy
Attn: Code 6101
Washington, D. C. 20360

Naval Ships R&D Laboratory
Annapolis Division
Attn: Code A800
Annapolis, Maryland 21402

Commanding Officer
Naval Ships R&D Center
Attn: Code 747
Washington, D. C. 20007

U. S. Naval Postgraduate School
Attn: Department of Chemistry
        and Material Science
Monterey, California 93940

Commander Naval Weapons Center
Naval Weapons Center
Attn: Code 5560
China Lake, California 93555

Commander
Naval Underseas Warfare Center
Pasadena, California 92152

Scientific Advisor
Commandant of the Marine Corps
Attn: Code AX
Washington, D. C. 20380

Commanding Officer
Army Research Office, Durham
Box CM, Duke Station
Attn: Metallurgy & Ceramics Div.
Durham, North Carolina 27706

Office of Scientific Research
Department of the Air Force
Attn: Solid State Div. (SRPS)
Washington, D. C. 20333

Defense Documentation Center
Cameron Station
Alexandria, Virginia 22314

National Bureau of Standards
Attn: Metallurgy Division
Washington, D. C. 20234

National Bureau of Standards
Attn: Inorganic Materials Div.
Washington, D. C. 20234

Atomic Energy Commission
Attn: Metals & Materials Branch
Washington, D. C. 20545

Argonne National Laboratory
Metallurgy Division
P. O. Box 299
Lemont, Illinois 60439

Brookhaven National Laboratory
Technical Information Division
Attn: Research Library
Upton, Long Island, New York 11973

Library
Bldg. 50, Room 134
Lawrence Radiation Laboratory
Berkeley, California 94720

Los Alamos Scientific Laboratory
P. O. Box 1663
Attn: Report Librarian
Los Alamos, New Mexico 87544

Commanding Officer
Army Materials and Mechanics
Research Center
Attn: Res. Programs Office (AMXMR-P)
Watertown, Massachusetts 02172

Director
Metals & Ceramics Division
Oak Ridge National Laboratory
P. O. Box X
Oak Ridge, Tennessee 37830

Commanding Officer
Naval Underwater Systems Center
Newport, Rhode Island 02844

Aerospace Research Laboratories
Wright-Patterson AFB
Building 450
Dayton, Ohio 45433

Defense Metals Information Center
Battelle Memorial Institute
505 King Avenue
Columbus, Ohio 43201

Army Electronics Command
Evans Signal Laboratory
Solid State Devices Branch
c/o Senior Navy Liaison Officer
Fort Monmouth, New Jersey 07703

Commanding General
Department of the Army
Frankford Arsenal
Attn: ORDBA-1320, 64-4
Philadelphia, Pennsylvania 19137

Executive Director
Materials Advisory Board
National Academy of Sciences
2101 Constitution Avenue, N. W.
Washington, D. C. 20418

NASA Headquarters
Attn: Code RRM
Washington, D. C. 20546

Air Force Materials Lab
Wright-Patterson AFB
Attn: MAMC
Dayton, Ohio 45433

Air Force Materials Lab
Wright-Patterson AFB
Attn: MAAM
Dayton, Ohio 45433

Deep Submergence Systems Project
Attn: DSSP-00111
Washington, D. C. 20360

Advanced Research Projects Agency
Attn: Director, Materials Science
Washington, D. C. 20301

Army Research Office
Attn: Dr. T. E. Sullivan
3045 Columbia Pike
Arlington, Virginia 22204

Department of the Interior
Bureau of Mines
Attn: Science & Engineering Advisor
Washington, D. C. 20240

Defense Ceramics Information Center
Battelle Memorial Institute
505 King Avenue
Columbus, Ohio 43201

National Aeronautics & Space Adm.
Lewis Research Center
Attn: Librarian
21000 Brookpark Rd.
Cleveland, Ohio 44135

Naval Missile Center
Materials Consultant
Code 3312-1
Point Mugu, California 93041

Commanding Officer
Naval Weapons Center Corona Labs.
Corona, California 91720

Commander
Naval Air Test Center
Weapons Systems Test Div. (Code 01A)
Patuxent River, Maryland 20670

Director
Ordnance Research Laboratory
P. O. Box 30
State College, Pennsylvania 16801

Director
Applied Physics Laboratory
Johns Hopkins University
8621 Georgia Avenue
Silver Spring, Maryland 20901

Director
Applied Physics Laboratory
1013 Northeast Fortieth St.
Seattle, Washington 98105

Materials Sciences Group
Code S130.1
271 Catalina Boulevard
Navy Electronics Laboratory
San Diego, California 92152

Dr. Waldo K. Lyon
Director, Arctic Submarine Laboratory
Code 90, Building 371
Naval Undersea R&D Center
San Diego, California 92132

Dr. R. Nathan Katz
Ceramics Division
U.S. Army Materials & Mechanics
    Research Center
Watertown, Mass. 02172

Lt. Cmdr. D. N. Hull
Chesapeake Division
Naval Facilities Engineering Command
Washington, D.C. 20390

Dr. John Norbutas
Code L63
Naval Civil Engineering Laboratory
Port Hueneme, Calif. 93043

Mr. Herbert C. Lamb
Naval Facilities Engineering Command
Code 032E
200 Stovall St.
Alexandria, Va. 22332

Dr. M. Yachnis
Naval Facilities Engineering Command
Code 04B
200 Stovall St.
Alexandria, Va. 22332

Professor R. Roy
Materials Research Laboratory
Pennsylvania State University
University Park, Pennsylvania   16802

Professor D. H. Whitmore
Department of Metallurgy
Northwestern University
Evanston, Illinois   60201

Professor J. A. Pask
Department of Mineral Technology
University of California
Berkeley, California   94720

Professor D. Turnbull
Div. of Engineering and Applied Sci.
Harvard University
Pierce Hall
Cambridge, Massachusetts   02100

Dr. T. Vasilos
AVCO Corporation
Research and Advanced Development Div.
201 Lowell St.
Wilmington, Massachusetts   01887

Dr. H. A. Perry
Naval Ordnance Laboratory
Code 230
Silver Spring, Maryland   20910

Dr. Paul Smith
Crystals Branch, Code 6430
Naval Research Laboratory
Washington, D. C.   20390

Dr. A. R. C. Westwood
RIAS Division
Martin-Marietta Corporation
1450 South Rolling Road
Baltimore, Maryland   21227

Dr. W. Haller
Chief, Inorganic Glass Section
National Bureau of Standards
Washington, D. C.   20234

Dr. R. H. Doremus
General Electric Corporation
Metallurgy and Ceramics Lab.
Schenectady, New York   12301

Professor G. R. Miller
Department of Ceramic Engineering
University of Utah
Salt Lake City, Utah   84112

Dr. Philip L. Farnsworth
Materials Department
Battelle Northwest
P. O. Box 999
Richland, Washington   99352

Mr. G. H. Heartling
Ceramic Division
Sandia Corporation
Albuquerque, New Mexico   87101

Mr. I . Berman
Army Materials and Mechanics
Research Center
Watertown, Massachusetts   02171

Dr. F. F. Lange
Westinghouse Electric Corporation
Research Laboratories
Pittsburgh, Pennsylvania   15235

Professor H. A. McKinstry
Pennsylvania State University
Materials Research Laboratory
University Park, Pa.   16802

Professor T. A. Litovitz
Physics Department
Catholic University of America
Washington, D. C.   20017

Dr. R. J. Stokes
Honeywell Corporate Research Center
10701 Lyndale Avenue South
Bloomington, Minnesota   55420

Dr. Harold Liebowitz
Dean of Engineering
George Washington Univeristy
Washington, D. C.   20006

Dr. H. Kirchner
Ceramic Finishing Company
P. O. Box 498
State College, Pennsylvania   16801

Professor A. H. Heuer
Case Western Reserve University
University Circle
Cleveland, Ohio   44106

Dr. D. E. Niesz
Battelle Memorial Institue
505 King Avenue
Columbus, Ohio   43201

Dr. F. A. Kroger
University of Southern California
University Park
Los Angeles, California   90007

Dr. Sheldon M. Wiederhorn
National Bureau of Standards
Inorganic Materials Division
Washington, D. C.   20234

Dr. C. O. Hulse
United Aircraft Research Labs
United Aircraft Corporation
East Hartford, Connecticut   06108

Professor M. H. Manghnani
University of Hawaii
Hawaii Institute of Geophysics
2525 Correa Road
Honolulu, Hawaii 96822

Dr. Stephen Malkin
Department of Mechanical Engineering
University of Texas
Austin, Texas   78712

Prof. H. E. Wilhelm
Department of Mechanical Engineering
Colorado State University
Fort Collins, Colorado   80521

Stanford University
Dept. of Materials Sciences
Stanford, California   94305

Dr. R. K. MacCrone
Department of Materials Engineering
Rensselaer Polytechnic Institute
Troy, New York   12181

Dr. D. C. Mattis
Belfer Graduate School of Science
Yeshiva University
New York, New York   10033

Professor R. B. Williamson
College of Engineering
University of California
Berkeley, California   94720

Professor R.. W. Gould
Department of Metallurgical
   and Materials Engineering
College of Engineering
University of Florida
Gainesville, Florida   32601

Professor V. S. Stubican
Department of Materials Science
Ceramic Science Section
Pennsylvania State University
University Park, Pennsylvania   16802

Dr. R. C. Anderson
General Electric R&D Center
P. O. Box 8
Schenectady, New York   12301

Dr. Bert Zauderer
MHD Program, Advanced Studies
Room L-9513-VFSC
General Electric Company
P. O. Box 8555
Philadelphia, Pennsylvania   19101

Prof. C. F. Fisher, Jr.
Department of Mechanical and Aero-
   space Engineering
University of Tennessee
Knoxville, Tennessee   37916

41

U.S. DEPT. OF COMM. BIBLIOGRAPHIC DATA SHEET	1. PUBLICATION OR REPORT NO. NBSIR 74-512	2. Gov't Accession No.	3. Recipient's Accession No.
4. TITLE AND SUBTITLE The Proof Testing of Porcelain Insulators and the Application of Acoustic Emission			5. Publication Date June 1974
			6. Performing Organization Code
7. AUTHOR(S) A. G. Evans, S. M. Wiederhorn, M. Linzer, and E. R. Fuller, Jr.			8. Performing Organ. Report No. NBSIR 74-512
9. PERFORMING ORGANIZATION NAME AND ADDRESS NATIONAL BUREAU OF STANDARDS DEPARTMENT OF COMMERCE WASHINGTON, D.C. 20234			10. Project/Task/Work Unit No. 3130451
			11. Contract/Grant No. PO-3-0072
12. Sponsoring Organization Name and Complete Address (Street, City, State, ZIP) Naval Civil Engineering Laboratory Port Hueneme, California 93043			13. Type of Report & Period Covered Final Report
			14. Sponsoring Agency Code

15. SUPPLEMENTARY NOTES

To be published in the Journal of The American Ceramic Society

16. ABSTRACT (A 200-word or less factual summary of most significant information. If document includes a significant bibliography or literature survey, mention it here.)

An investigation of proof testing has been conducted on large cone and post porcelain insulators. The cone configuration was found to be unsuitable for overload proof testing to the loads needed for effective lifetime predictions. The only merit of subjecting this configuration to a proof test is the assurance of no immediate macrocracking during installation. This is achieved by testing to a load marginally larger than the service load. Conversely, the post configuration was found to exhibit the basic prerequisites for effective proof testing; but detailed stress analysis of this system is needed before specific proof testing procedures can be recommended. Finally, acoustic emission measurements were found to be a major asset for monitoring both macrocracking events and stress development during the proof tests.

17. KEY WORDS (six to twelve entries; alphabetical order; capitalize only the first letter of the first key word unless a proper name; separated by semicolons)

Acoustic emission; macrocracking; porcelain insulators; proof testing; residual strain.

18. AVAILABILITY ☐ Unlimited	19. SECURITY CLASS (THIS REPORT) UNCLASSIFIED	21. NO. OF PAGES 42
☒ For Official Distribution. Do Not Release to NTIS		
☐ Order From Sup. of Doc., U.S. Government Printing Office Washington, D.C. 20402, <u>SD Cat. No. C13</u>	20. SECURITY CLASS (THIS PAGE)	22. Price
☐ Order From National Technical Information Service (NTIS) Springfield, Virginia 22151	UNCLASSIFIED	